RESEARCH ARTICLE

Hydrolytic Expansion Induces Corrosion Propagation for Increased Fe Biodegradation

Cijun Shuai[1,2,3], Sheng Li[1], Shuping Peng[4], Youwen Yang[2], Chengde Gao[1]*

[1]State Key Laboratory of High-Performance Complex Manufacturing, College of Mechanical and Electrical Engineering, Central South University, Changsha 410083, China

[2]Institute of Bioadditive Manufacturing, Jiangxi University of Science and Technology, Nanchang 330013, China

[3]Shenzhen Institute of Information Technology, Shenzhen 518172, China

[4]The Key Laboratory of Carcinogenesis of the Chinese Ministry of Health, Xiangya Hospital, Central South University, Changsha, 410008, China

Abstract: Fe is regarded as a promising bone implant material due to inherent degradability and high mechanical strength, but its degradation rate is too slow to match the healing rate of bone. In this work, hydrolytic expansion was cleverly exploited to accelerate Fe degradation. Concretely, hydrolyzable Mg_2Si was incorporated into Fe matrix through selective laser melting and readily hydrolyzed in a physiological environment, thereby exposing more surface area of Fe matrix to the solution. Moreover, the gaseous hydrolytic products of Mg_2Si acted as an expanding agent and cracked the dense degradation product layers of Fe matrix, which offered rapid access for solution invasion and corrosion propagation toward the interior of Fe matrix. This resulted in the breakdown of protective degradation product layers and even the direct peeling off of Fe matrix. Consequently, the degradation rate for Fe/Mg_2Si composites (0.33 mm/y) was significantly improved in comparison with that of Fe (0.12 mm/y). Meanwhile, Fe/Mg_2Si composites were found to enable the growth and proliferation of MG-63 cells, showing good cytocompatibility. This study indicated that hydrolytic expansion may be an effective strategy to accelerate the degradation of Fe-based implants.

Keywords: Hydrolytic expansion, Biodegradation, Fe-based implants, Selective laser melting, Cytocompatibility

***Corresponding Author:** Chengde Gao, State Key Laboratory of High-Performance Complex Manufacturing, College of Mechanical and Electrical Engineering, Central South University, Changsha 410083, China; gaochengde@csu.edu.cn.

Received: November 12, 2019; ***Accepted:*** January 2, 2020; ***Published Online:*** January 23, 2020

Citation: Shuai C, Li S, Peng S, *et al*., 2020, Hydrolytic expansion induces corrosion propagation for increased Fe biodegradation. *Int J Bioprint*, 6(1):248. DOI: 10.18063/ijb.v6i1.248

1 Introduction

Due to natural degradability, favorable mechanical properties, and acceptable biocompatibility, biodegradable metals have been extensively highlighted for fabricating bone implants over the past years[1-3]. Iron (Fe), which can corrode in the physiological environment, is considered as a typical biodegradable metal. Fe is especially attractive in load-bearing applications due to its high mechanical strength. The applications of Fe as bone implants have been validated by animal experiments and no acute inflammatory reaction, systemic, or local toxicity were reported, indicating good biocompatibility[4-7]. However, Fe still stays intact *in vivo* even after 6 months, which indicates that a fast corrosion rate is urgently demanded[8].

To increase the corrosion rate of Fe, lots of researches, for example, alloying, surface treatment, and new fabrication process have been carried out[9]. Hermawan *et al*. added manganese (Mn) into Fe to reduce the corrosion potentials of Fe, thereby increasing the corrosion rates[10]. Subsequently,

Schinhammer *et al*. introduced palladium (Pd) into Fe−Mn alloy and found that Pd accelerated Fe degradation through micro-galvanic corrosion[11]. Zhou *et al*. prepared silicon carbide (SiC) thin films on the Fe surface through sandblasting treatment[12]. They found that surface morphology, surface composition, and surface area of Fe were changed, causing higher weight loss. Moravej *et al*. fabricated Fe implants by electroforming and evaluated the degradation behavior *in vitro*[13]. This process increased structural defects of Fe, which was responsible for the fast corrosion. These Fe-based implants exhibit a faster degradation rate than Fe in the physiological environment. However, as the degradation proceeds, corrosion products will gradually accumulate on the substrate, forming dense protective layers due to their low solubility. This inevitably impedes or even insulates the contact between the solution and the matrix, resulting in a slow degradation at the later stage of degradation[12].

Magnesium silicide (Mg_2Si) is a common biomaterial with favorable biocompatibility, and both of silicon (Si) and magnesium (Mg) are essential elements in the human body, as reported by Jiang *et al*.[14] Due to the high chemical activity, Mg_2Si can rapidly react with H_2O, releasing expansive gases[15]. This prompts us to contemplate that if Mg_2Si is introduced into the Fe matrix, the rapid hydrolysis of Mg_2Si will expose more area of Fe matrix to the physiological environment. More importantly, the escaped gases resulted from Mg_2Si hydrolysis may penetrate the dense degradation product layers, which is expected to solve the above-mentioned problem induced by dense degradation product layers, thereby endowing the Fe-based implant a rapid degradation throughout the degradation process.

In this work, hydrolyzable Mg_2Si was cleverly exploited to accelerate Fe degradation. Fe/Mg_2Si composites were prepared through selective laser melting process, which was also known as one kind of three-dimensional (3D) printing techniques[16,17]. Moving laser can irradiate powder bed with a rapid solidification rate compared with traditional method[18,19], which was beneficial for ensuring the relative phase stability of samples, which may be due to the rapid melting and solidification process (with a cooling rate of $10^3 – 10^6$°C/s), as pointed out by Yu *et al*.[20] Moreover, Dadbakhsh *et al*. stated that selective laser melting possessed an exceptional flexibility to manufacture composites with a uniform dispersion of secondary phase due to laser-based and layer-by-layer natures, simultaneous powder metallurgy[21-23]. Besides, selective laser melting is well known for the capability of directly preparing 3D parts with precise shape[24-29]. This paper aimed to present a systematic study that investigated the degradability of selective laser melting derived Fe/Mg_2Si composites based on their composition variation. The microstructure and mechanical properties of the composites were investigated for bone implant applications. In addition, cytocompatibility was also systematically evaluated. This study covered processes of 3D printing technologies, property evaluations of printed implants, interactions of MG-63 cells, the composites, etc.

2 Materials and methods

2.1 Materials

Fe powder with a purity of 99.9% was purchased from Wuxi Sairui metal powder manufacturing Co., Ltd. (Jiangsu, China). The powder particle size was characterized by laser particle analyzer (Malvern 3000, UK). Mg_2Si powder was obtained from Shanghai Xianxin New Material Technology Co., Ltd. The Mg_2Si powder was milled to get a small particle size at a speed of 200 rpm for 3 h in a planetary ball mill, and the stainless steel ball to powder ratio was 1:1. Subsequently, Mg_2Si powder with different mass ratio (0, 0.3, 0.6, 0.9, and 1.2 wt.%) was mixed with Fe powder using mechanical stirring followed by milling at a speed of 200 rpm for 60 min after optimization of the main parameters of mixing time and rotation rate. These mixing parameters were beneficial for relatively better powder mixing performance[30,31].

2.2 Sample preparation

Fe/Mg_2Si composites were prepared by a selective laser melting system, which was composed of a laser melting platform, control system, and lifting

platform[32,33]. The specific laser melting procedure was as follows: (1) Fe/Mg_2Si powders were put on the laser melting platform; (2) Fe/Mg_2Si powders was selectively melted by laser beam; (3) after laser melting, a descending height was achieved through the lifting platform; (4) the steps of (1) – (3) were continually repeated until the Fe/Mg_2Si composites were completely prepared; and (5) an air compressor was used for scrubbing samples and removing residual powder. In this study, the laser scan rate of 24 mm/s, layer thickness of 100 μm, and laser power of 90 W were used as the melting parameters for good formality during experiments.

2.3 Microstructural characterization

Fe/Mg_2Si composites were mechanically polished, thereafter ultrasonically cleaned in ethanol. After etching in 4% HNO_3 alcohol solution for 40 s, the metallographic microstructure of Fe/Mg_2Si composites was observed using an Olympus optical microscope (PMG-3, Japan). The surface morphology was characterized by a XL-30FEG scanning electron microscopy (SEM, Philips, the Netherlands), and the elemental compositions were determined by energy-dispersive X-ray spectroscopy (EDS). The phase analysis of Fe/Mg_2Si composites was performed by a Siemens X-ray diffractometer (XRD, D5000, Germany) with a scanning speed of 8/min from 20° to 90° of scattering angles.

2.4 Mechanical tests

The mechanical properties of Fe/Mg_2Si composites were determined by compression, bending, and hardness tests. The compression tests were performed on a Zhongluchang Universal Tester (Model WDW-10H, China) at a strain rate of 0.05 mm/s according to the ASTM E9-09 standard[34]. The prepared Fe/Mg_2Si samples were circular cylinder with a diameter of 8 mm and a height of 12 mm. As all the samples were ductile, compression strength was determined by the stress at a strain of 30%[34]. Three-point bending tests were performed at a speed of 0.05 mm/s on the Zhongluchang Universal Tester (Model WDW-10H, China). The span of the bending tests was 12 mm between the two supporting points. Hardness tests were carried out using micro-indentation tester (Shanghai Taiming Optical Instrument Co. Ltd., China) with a dwell time of 10 s. For each group, at least four measurements were carried out to acquire accurate average values.

2.5 Electrochemical tests

The electrochemical behaviors of Fe/Mg_2Si composites were tested by an IM6 electrochemical workstation (Zahner, Germany) in simulated body fluid (SBF) at 37°C. The SBF with a pH of 7.4 contained 8.035 $g \cdot L^{-1}$ NaCl, 0.225 $g \cdot L^{-1}$ KCl, 0.311 $g \cdot L^{-1}$ $MgCl_2 \cdot 6H_2O$, 0.231 $g \cdot L^{-1}$ $K_2HPO_4 \cdot 3H_2O$, 6.118 $g \cdot L^{-1}$ $(CH_2OH)_3CNH_2$, 0.355 $g \cdot L^{-1}$ $NaHCO_3$, 0.292 $g \cdot L^{-1}$ $CaCl_2$, and 0.072 $g \cdot L^{-1}$ Na_2SO_4[2,35]. The typical three-electrode cell, containing the saturated calomel electrode (SCE, reference electrode), the sample (working electrode), and the platinum electrode (auxiliary electrode), was used to perform electrochemical tests. The potentiodynamic polarization curves of samples were obtained at a rate of 0.25 mV/s (−1200 – 100 mV) in SBF. The corrosion current density (I_{corr}) of samples was calculated by tafel extrapolation of the anodic and cathodic part of the polarization curves. Afterward, the I_{corr} was converted into the electrochemical corrosion rates based on the ASTM G59 standard[36,37]. The surface morphologies of the samples were examined using a Wyko NT9100 optical profiler (VEECO, USA) and the surface roughness value (*Ra*) was simultaneously acquired by the average standard deviation of height values.

2.6 Immersion tests

The immersion tests of Fe/Mg_2Si composites were performed to study the degradation behavior, including corrosion rates, corrosion morphologies, and surface composition. The immersion tests were carried out in SBF[38]. According to the ASTM-G31-72, Fe/Mg_2Si samples with an exposed surface (cm^2) to SBF (ml) ratio of 1:15 were separately immersed at 37°C[3,39]. After immersion for 21 days, the samples were first rinsed with deionized water and ethanol, and then dried in hot air. The cross-sectional morphologies were observed using SEM.

Meanwhile, the composition analysis of corrosion products was performed by EDS. The degradation rates of samples were calculated according to the methods in the literature[35].

2.7 Cytocompatibility tests

Human osteosarcoma cell line (MG-63) from the American Type Culture Collection was adopted to evaluate the cytocompatibility of samples according to the indirect contact method[4,40]. The MG-63 cells were first cultured in Dulbecco's Modified Eagle's Medium (DMEM) with 100 U/ml penicillin, 100 mg/ml streptomycin, and 10% fetal bovine serum at 37°C under a humidified atmosphere of 5% CO_2. The Fe/Mg_2Si samples were immersed in DMEM for 3 days with a surface area/solution ratio of 1.25 (cm^2/ml) at 37°C according to the ISO 10993-12[1]. Subsequently, the supernatant fluid was withdrawn and centrifuged for preparing the extract. For fluorescence staining assay, MG-63 cells were incubated in the extracts of different concentrations (25, 50, and 100%) with DMEM as the control group (extract concentration of 0%) for 1, 2, and 3 days, respectively. The MG-63 cells were subsequently stained by ethidium homodimer-1 reagents and calcein-AM for 18 min, and finally rinsed twice using phosphate-buffered solution. To observe the living cells, the cells were fixed on glasses and checked using a BX60 Fluorescence Microscope (Olympus, Japan). The number of living cells was estimated by ImageJ software according to the fluorescent images. To evaluate the viability of MG-63 cells in the extracts of different concentrations (0, 25, 50, and 100%), CCK-8 tests were performed for 1, 2, and 3 days, respectively. After culture for the scheduled time, 10 μL CCK-8 solutions (5 mg/ml) were added to the cell culture medium. Then, the absorbance was gained by a microplate reader (BioRad, USA) at 450 nm. Cell viability was calculated since it was positively correlated with the absorbance[41].

2.8 Statistical analysis

Experimental data were presented as mean ± standard deviation. Symbol "*" indicates a significant difference ($P < 0.05$).

3 Results and discussion

3.1 Powder characterization and sample preparation

The used powders in this study are depicted in **Figure 1A-F**. SEM images in **Figure 1A,B** indicated that both Fe and Mg_2Si powders had an irregular shape and the latter exhibited smaller particle sizes than the former. The particle size distribution of Fe powder was further measured by a laser particle analyzer. It is shown in **Figure 1A** that the particle size of Fe powder was mainly between 12 and 30 μm and the average value was 27.1 ± 0.5 μm. Meanwhile, fine Mg_2Si particles were evenly distributed in Fe powder in **Figure 1C**, which enabled Mg_2Si to fully exert its roles in the composite. Besides, XRD patterns in **Figure 1E** showed that the only detectable phase was α-Fe with BCC structure and the (110) crystal plane had the highest intensity due to the preferred crystalline orientation. For Mg_2Si powder, the Mg_2Si phase was identified by main diffraction peaks at 24.2°, 40.1°, and 47.3° corresponding to (111), (220), and (311) diffraction planes, respectively, as illustrated in **Figure 1E**. EDS analysis in **Figure 1F** showed that Fe and Mg_2Si powders were composed of Fe and Mg, Si elements, respectively, which indicated higher purity of the powders. The mixed powders of Fe and Mg_2Si were scanned by laser according to the computer-aided design model to prepare composites, as illustrated in **Figure 1G**. It could be found that the prepared composites have uniformly distributed porous structures with a diameter of 0.8 mm. The porous structures of composites would not only accelerate Fe degradation through the increase of surface area in contact with SBF but also promote nutrient transport through the interconnected architecture.

3.2 Microstructure

The microstructural features of Fe/Mg_2Si composites are presented in **Figure 2**. It is shown in **Figure 2A,E** that the Fe/0.3Mg_2Si had a compact microstructure without original powder particles. Meanwhile, a small amount of Mg_2Si could be discernible, as evidenced by EDS

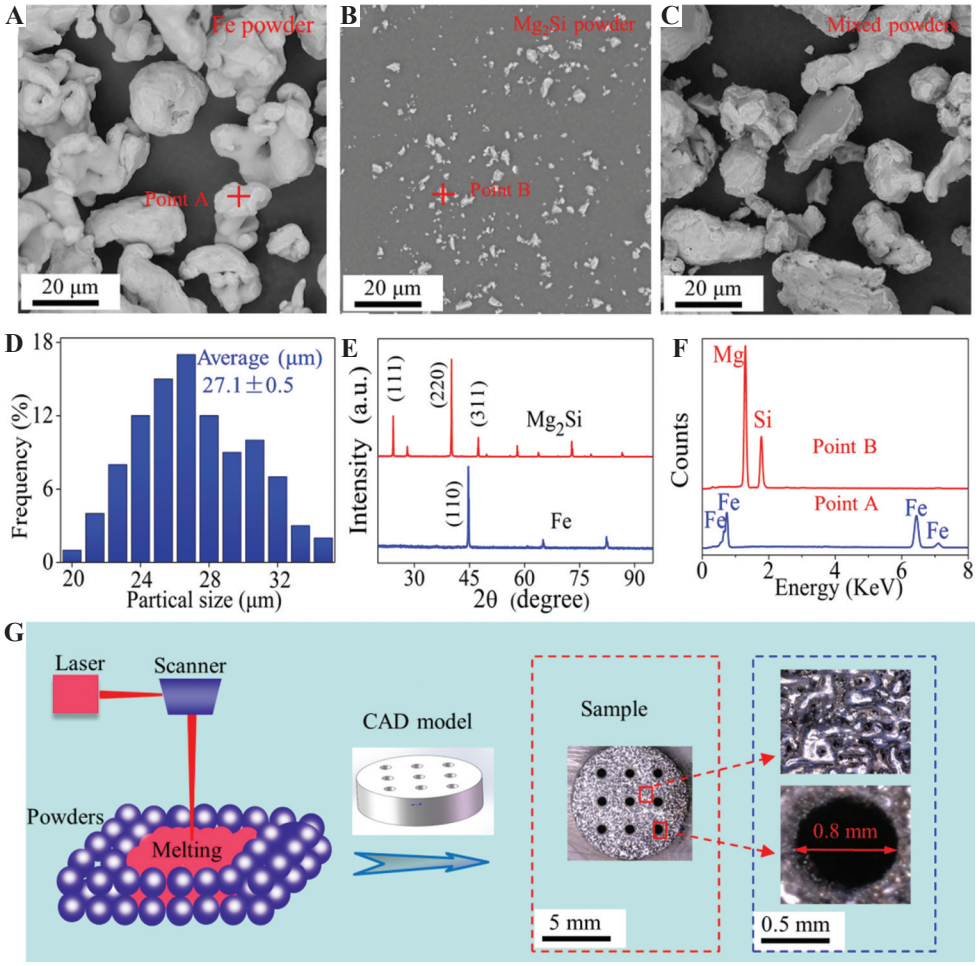

Figure 1. (A-C) The morphologies, (D) particle size distribution, (E) XRD patterns, and (F) EDS analysis of Fe and/or Mg_2Si powders. (G) Schematic illustration of the laser melting process for sample preparation. The prepared composites had a uniformly distributed porous structure (the pore diameter of 0.8 mm).

analysis in **Figure 2I**. Fe/0.6Mg_2Si in **Figure 2B,F** exhibited similar microstructural features with Fe/0.3Mg_2Si except for a slightly higher Mg_2Si content. Fe/0.9Mg_2Si in **Figure 2C,G** showed two distinct phases in the microstructure, in which the black phase was Mg_2Si and the grey phase was Fe matrix. Moreover, Fe/0.9Mg_2Si also showed the uniformly distributed Mg_2Si within the matrix. Therefore, it was reasonably expected that the Fe/Mg_2Si composite would possess uniform bulk property. However, when the additional content of Mg_2Si was 1.2 wt.%, micropores were found, as exhibited in **Figure 2D,H**. The micropores may be caused by interconnected Mg_2Si by EDS analysis **Figure 2J,K** as a result of the inhomogeneous distribution. The interconnected Mg_2Si tended to merge and form large clusters, which hindered the bonding of liquid Fe, leading to micropores. Micropores as microstructure defects may become stress concentration points, resulting in deteriorated mechanical properties and local corrosion, especially in the corrosive physiological environment containing chloride ion. This was similar to other studies on the microstructural features of Fe/ceramic composites[34].

The water contact angles of Fe/Mg_2Si composites as well as Fe are shown in **Figure 3a**. The sequence of water contact angle from low to high was: Fe/1.2Mg_2Si (60.11 ± 2.1°) < Fe/0.9Mg_2Si (61.08 ± 1.8°) < Fe/0.6Mg_2Si (62.95 ± 2.2°) < Fe/0.3Mg_2Si (65.24 ± 2.5°) < Fe (68.74 ± 3.1°). Usually, the smaller the

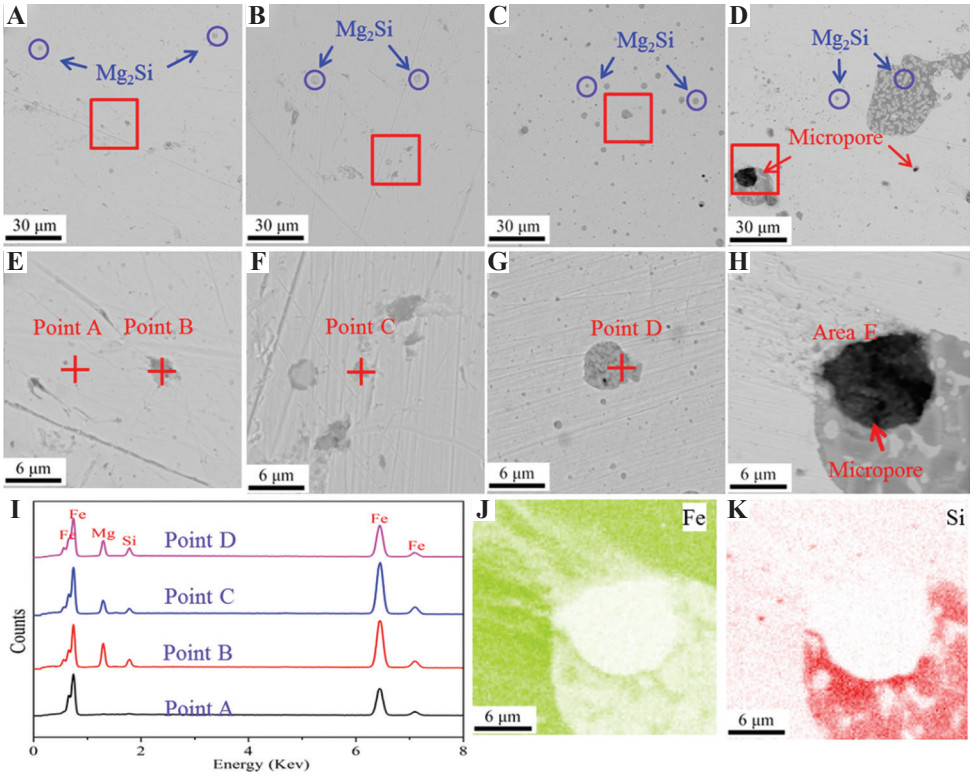

Figure 2. Low- and high-magnification SEM images of (A,E) Fe/0.3Mg_2Si, (B,F) Fe/0.6Mg_2Si, (C,G) Fe/0.9Mg_2Si, and (D,H) Fe/1.2 Mg_2Si composites and corresponding EDS analysis of (I) point A-D and (J,K) area E.

contact angle is, the better the hydrophilicity will be. This indicated that Fe/Mg_2Si had stronger hydrophilicity than Fe. It is considered that high hydrophilicity is of significance for bone implants, which contributes to corrosion attack in the physiological environment[38].

The XRD patterns of Fe/Mg_2Si composites are given in **Figure 3B**. It could be found from the figure that the detectable phase was α-Fe for all the Fe/Mg_2Si composites, which was similar to that of Fe powder in **Figure 1E**. Moreover, there were no obvious changes in the peak positions and relative intensities. The Mg_2Si peaks could not be found for all the samples, which attributed to the low contents. The metallographic micrographs of Fe/Mg_2Si composites are presented in **Figure 3C**. It was seen that Fe/0.3Mg_2Si exhibited flexuous grain boundaries with grain sizes ranging from 5 to 45 μm (average grain size of 29.8 ± 2.1 μm). The Fe/0.6Mg_2Si consisted of grain sizes ranging from 5 to 35 μm and its average grain size was 23.7 ± 1.5 μm. The grains of Fe/0.9Mg_2Si were obviously refined with an average grain size of 18.6 ± 1.2 μm. The grains of Fe/1.2Mg_2Si also exhibited a smaller size (average grain size of 21.1 ± 1.8 μm) in comparison with Fe/0.3Mg_2Si. However, the micropores on surfaces of Fe/1.2Mg_2Si were discernible due to the relatively large amounts of Mg_2Si.

3.3 Mechanical properties

Functionally speaking, the compression strength of bone implants was thought to be an important indicator since bones need to be strong enough to survive normal activities[42]. In this study, the compression strength of Fe/Mg_2Si composites is depicted in **Figure 4A**. It could be found that the compression strength gradually decreased (230 ± 15, 202 ± 20, 172 ± 12, 130 ± 10, and 88 ± 6 MPa for Fe, Fe/0.3Mg_2Si, Fe/0.6Mg_2Si, Fe/0.9Mg_2Si, and Fe/1.2Mg_2Si, respectively). The decreased compression strength could be attributed to the distributions and amounts of Mg_2Si, which may cause defects in the microstructure, as evidenced

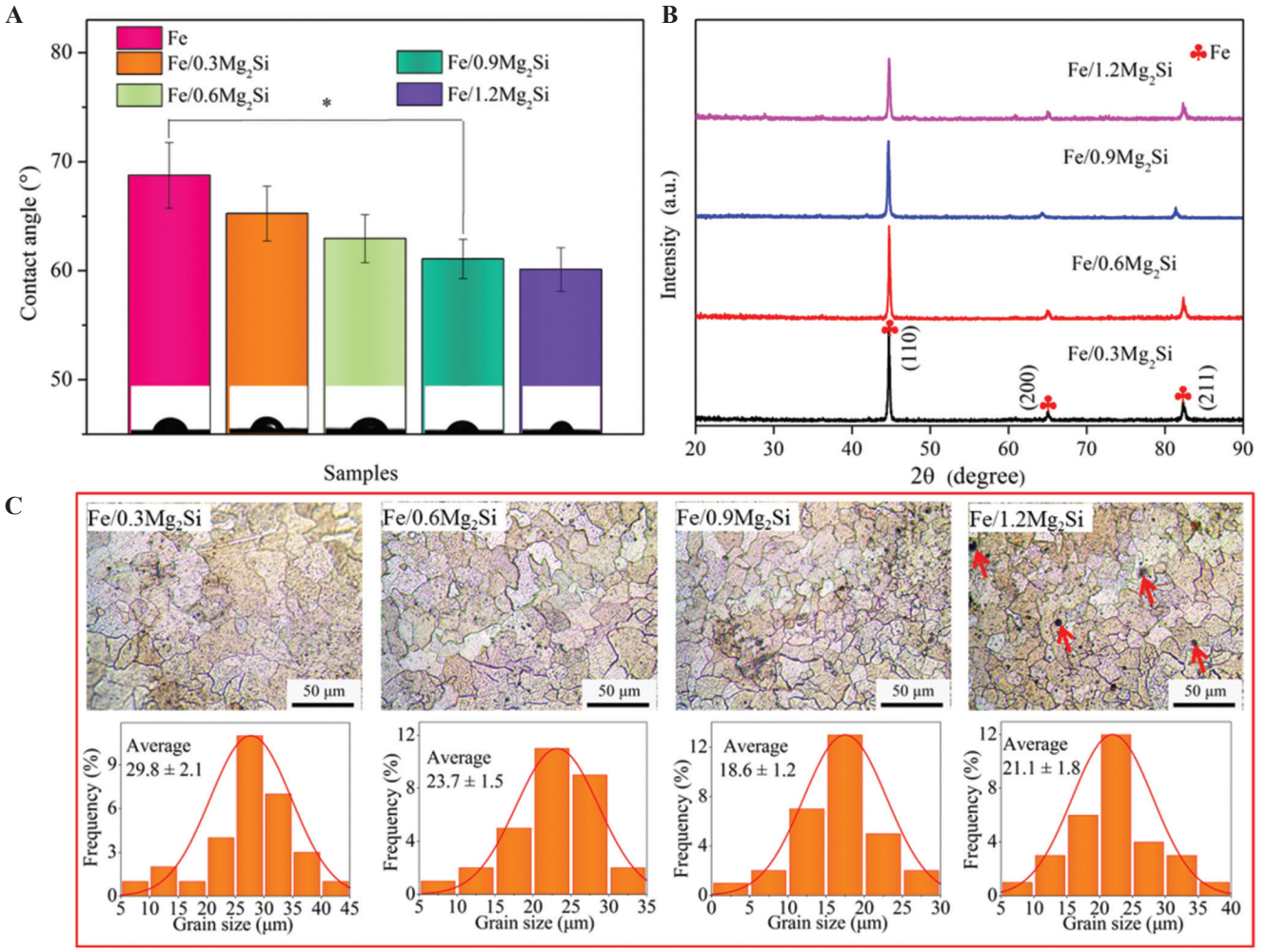

Figure 3. (A) Water contact angles, (B) XRD patterns, and (C) metallographic micrographs with corresponding grain size distributions of Fe/Mg_2Si composites. The micropores in the Fe/Mg_2Si composites were marked by red arrows.

in **Figure 2**. This phenomenon was similar to the previous study on the effects of hydroxyapatite on the compression strength of Fe-hydroxyapatite composite[43]. It was worth noting that the compression strength of human compact bone was between 90 and 170 MPa[44], which implied that the Fe/Mg_2Si composites still could provide adequate mechanical support for load-bearing applications. The modulus of fabricated Fe/Mg_2Si composites with the increasing Mg_2Si contents is shown in **Figure 4B**. It could be found from **Figure 4B** that the modulus gradually decreased with the increase in Mg_2Si. This phenomenon may be related to the increasing amount and dispersion patterns of the additive. Increasing Mg_2Si tended to form agglomerates and voids in the microstructure. Besides, the reduced modulus was also closely related to porous structures fabricated by selective laser melting. The modulus in this study could greatly alleviate biomechanical mismatch during the new bone remodeling process, thereby eliminating the problem of stress shielding between bone and implants. In addition, it is shown in **Figure 4C** that the sequence of bending strength from high to low was: Fe > Fe/0.3Mg_2Si > Fe/0.6Mg_2Si > Fe/0.9Mg_2Si > Fe/1.2Mg_2Si composite, which was consistent with the sequence of the compression strength.

In addition, the measured hardness by micro-indentation tester is exhibited in **Figure 4D**. It could be found that the hardness of Fe/0.9Mg_2Si sample (145 ± 9 HV) was higher than other

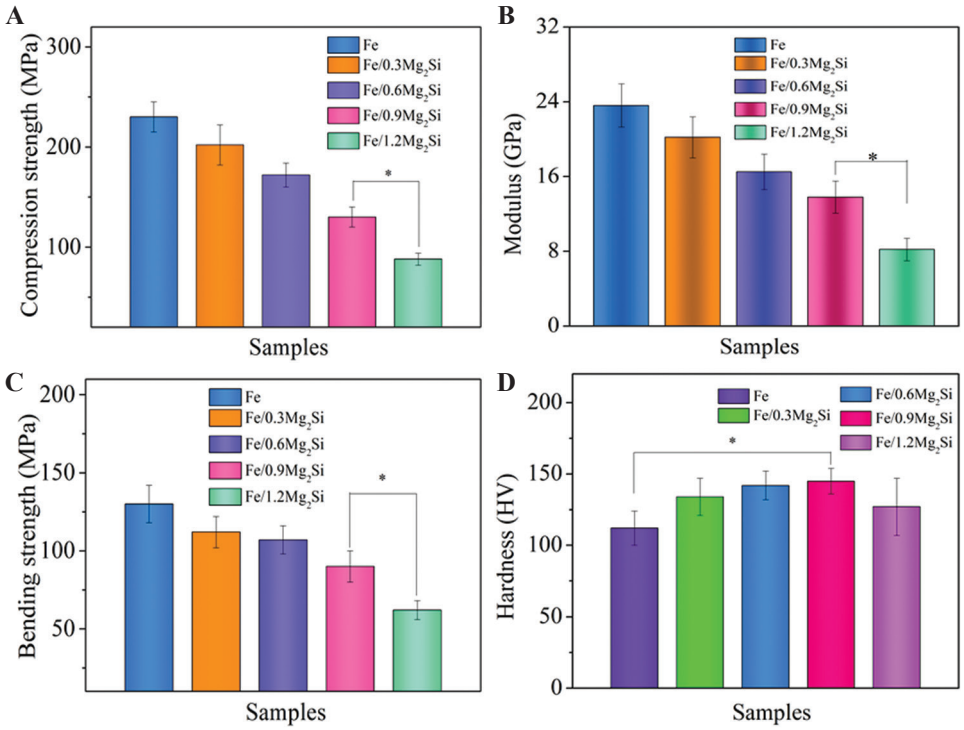

Figure 4. (A) Compression strength, (B) elastic modulus, (C) bending strength, and (D) hardness of Fe/Mg_2Si composites with Fe as a control group. *$P < 0.05$.

samples (112 ± 12, 134 ± 13, 142 ± 10, and 127 ± 20 HV for Fe, Fe/0.3Mg_2Si, Fe/0.6Mg_2Si, and Fe/1.2Mg_2Si, respectively). It was also worthy to note that a decrease in hardness was observed in Fe/1.2Mg_2Si. Both too high amount and uneven distribution of Mg_2Si would merge and hinder the liquid Fe phase bonding, leading to the formation of micropores, thereby reducing the hardness of Fe/1.2Mg_2Si composite. This was also evidenced by the large standard deviation in **Figure 4D**.

3.4 Electrochemical behaviors

Potentiodynamic polarization curves were useful tools to measure the instantaneous corrosion of samples. The polarization curves of Fe/0.3Mg_2Si, Fe/0.6Mg_2Si, Fe/0.9Mg_2Si, and Fe/1.2Mg_2Si composites with Fe as a control group are shown in **Figure 5A** and I_{corr} was determined from abscissa of intersection from tafel extrapolation. I_{corr} for Fe, Fe/0.3Mg_2Si, Fe/0.6Mg_2Si, Fe/0.9Mg_2Si, and Fe/1.2Mg_2Si was 12.58 ± 3.5, 19.95 ± 4.2, 27.54 ± 4.7, 39.81 ± 4.6, and 50.11 ± 4.9 μA/cm^2, respectively. The increase in I_{corr} indicated aggravated corrosion of composites with the addition of Mg_2Si. Meanwhile, a higher I_{corr} corresponded to worse corrosion resistance and a higher electrochemical corrosion rate. According to **Figure 5B**, the average electrochemical corrosion rates of Fe, Fe/0.3Mg_2Si, Fe/0.6Mg_2Si, Fe/0.9Mg_2Si, and Fe/1.2Mg_2Si were determined as 0.15, 0.24, 0.33, 0.48, and 0.61 mm/y, respectively, indicating that the addition of Mg_2Si accelerated Fe corrosion. The extent of metal corrosion on the surface after potentiodynamic polarization tests could be characterized by corrosion morphology. The stronger the corrosion was, the more severe the surface damage was. The surface profiles of Fe/0.3Mg_2Si, Fe/0.6Mg_2Si, Fe/0.9Mg_2Si, and Fe/1.2Mg_2Si with Fe as a control group were observed by an optical profiler and depicted in **Figure 5C-G**, in which red meant surface with large height and blue meant deep depression caused by corrosion. Besides, the calculated surface roughness value (*Ra*) is shown in **Figure 5H**. It could be found that there were obvious differences between the surface profiles of Fe/Mg_2Si and Fe. Fe remained relatively intact and most surfaces

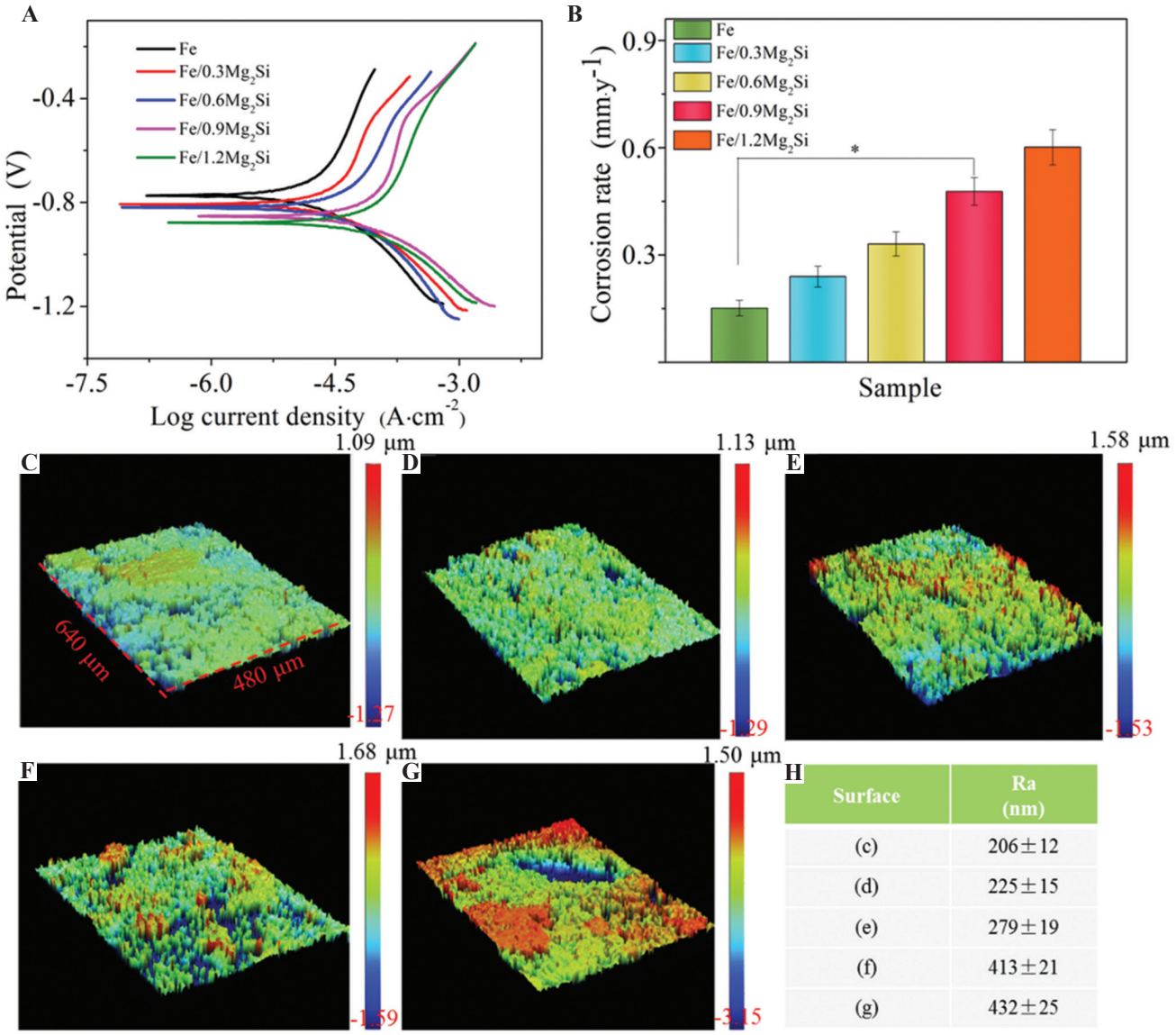

Figure 5. (A) Potentiodynamic polarization curves of Fe/Mg_2Si composites with Fe as a control group and (B) the corresponding electrochemical corrosion rates determined from tafel extrapolation. The representative surface profiles of (C) Fe, (D) Fe/0.3Mg_2Si, (E) Fe/0.6Mg_2Si, (F) Fe/0.9Mg_2Si, (G) Fe/1.2Mg_2Si, and (H) average surface roughness (*Ra*).

were even and smooth after polarization tests. Fe/0.3Mg_2Si presented a relatively smooth surface with a *Ra* value of 225 ± 15 nm. Enhanced corrosion of Fe/0.6Mg_2Si brought about an increase in *Ra* value of 279 ± 19 nm. Fe/0.9Mg_2Si revealed relatively rough surface morphologies with a high *Ra* value of 413 ± 21 nm. Fe/1.2Mg_2Si was characterized by inhomogeneous corrosion with a *Ra* value of 432 ± 25 nm and corrosion holes.

3.5 Immersion tests

The corrosion morphologies of Fe/Mg_2Si and Fe surface after immersion tests for 21 days in SBF at 37°C are depicted in **Figure 6**. The surface of Fe was corroded and a few corrosion products were present on its surface, as shown in **Figure 6A**. Fe/0.3Mg_2Si and Fe/0.6Mg_2Si in **Figure 6B,C** suffered relatively severe corrosion in comparison with that of Fe. Fe/0.9Mg_2Si and Fe/1.2Mg_2Si

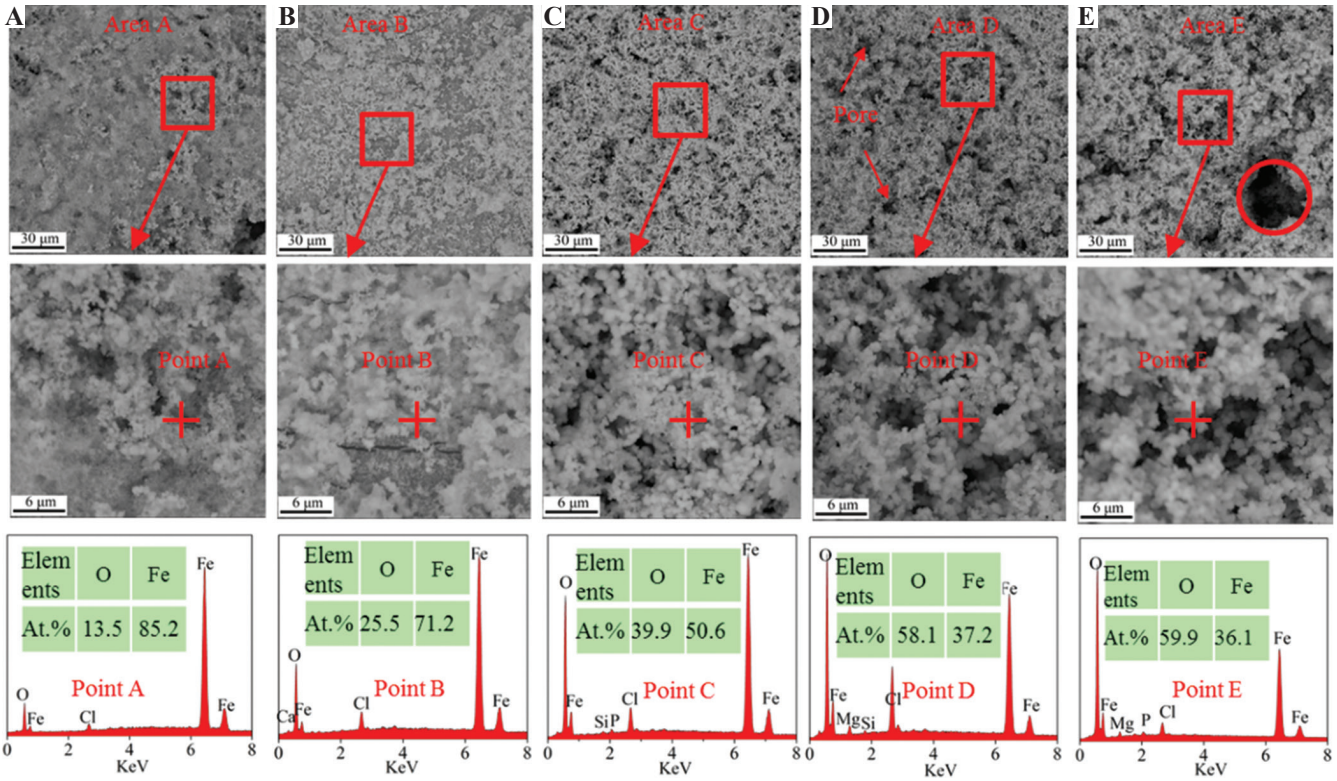

Figure 6. The surface morphologies of (A) Fe, (B) Fe/0.3Mg_2Si, (C) Fe/0.6Mg_2Si, (D) Fe/0.9Mg_2Si, and (E) Fe/1.2Mg_2Si at low- and high-magnifications after 21 days immersion in SBF. EDS analysis of corrosion products was performed to reveal the elemental ratios of O/Fe.

suffered the most severe corrosion, as evidenced by the existence of many more corrosion products in **Figure 6D,E**. Moreover, a few pores were present in the corrosion layers, which indicated that the corrosive SBF penetrated into the matrix through the degradation of product layers. In other words, the corrosion products were not as passive as that of Fe. Meanwhile, EDS analysis of corrosion products revealed that the elemental ratio of O/Fe became higher with the increase of Mg_2Si, also indicating that Fe corrosion was more severe. However, local corrosion was found for Fe/1.2Mg_2Si, as evidenced by the circle in **Figure 6E**, which may deteriorate the mechanical properties during the degradation process. Local corrosion for Fe/1.2Mg_2Si may be closely related to the presence of micropores in its microstructure.

To gain insight into the corrosion process of Fe/Mg_2Si composites in SBF, their cross-sectional morphologies after 21 days of immersion were investigated by SEM and the elemental compositions were analyzed by EDS (**Figure 7**). It could be found from **Figure 7A** that there were dense degradation product layers on Fe matrix, and the interface between Fe matrix and the degradation product layers was obvious. The dense degradation product layers provided good protection effects on Fe in SBF, which inhibited corrosion propagation toward the interior of Fe matrix. The introduction of Mg_2Si significantly changed the cross-sectional morphology of Fe. For Fe/0.3Mg_2Si, cracks were present in the degradation of product layers in **Figure 7B**, which promoted SBF penetration. For Fe/0.6Mg_2Si, the degradation of product layers was more porous and loose than that of Fe/0.3Mg_2Si, as shown in **Figure 7C**. For Fe/0.9Mg_2Si and Fe/1.2Mg_2Si in **Figure 7D,E**, the degradation of product layers had many tiny and narrow openings exposed toward the outside surface. In addition, EDS analysis of Points A, B, and C in **Figure 7D,E** indicated that the gray region was Fe matrix and the black region was the degradation products containing O, Fe, and Si. The presence of these

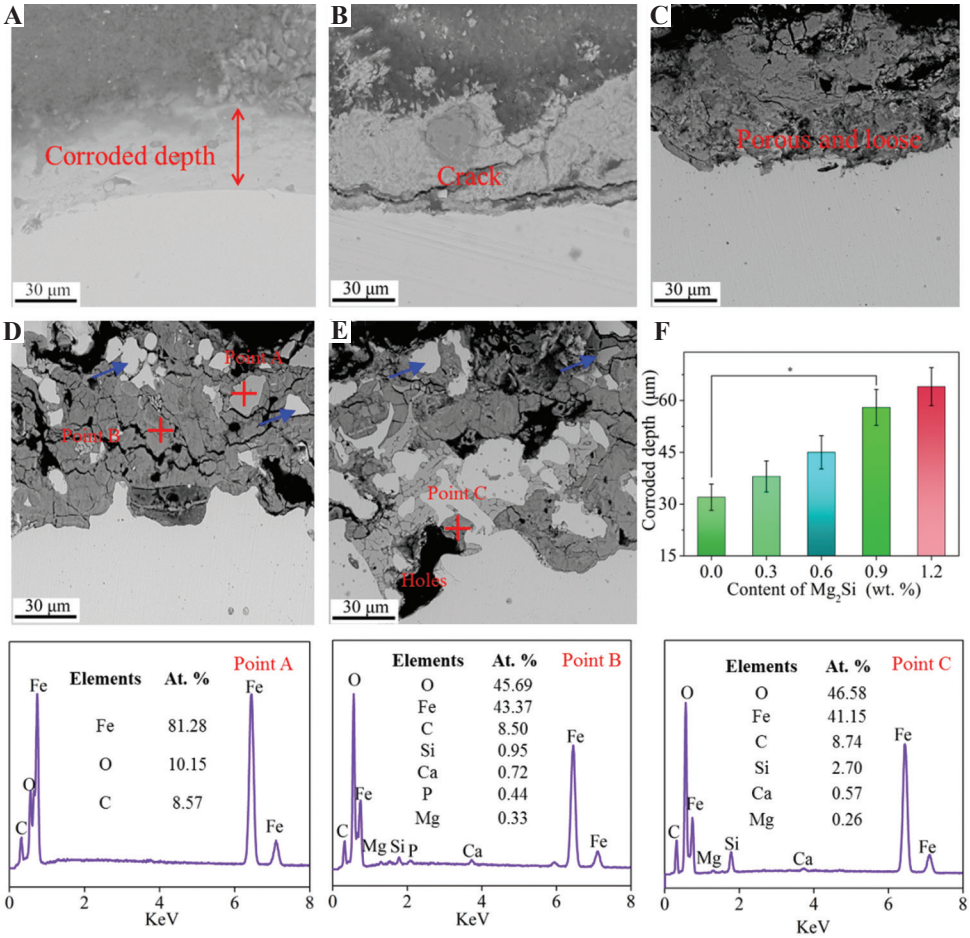

Figure 7. SEM images showing the typical cross-sectional morphologies of (A) Fe, (B) Fe/0.3Mg_2Si, (C) Fe/0.6Mg_2Si, (D) Fe/0.9Mg_2Si, (E) Fe/1.2Mg_2Si with corresponding EDS analysis of Points A, B, and C. (F) Corroded depth of Fe/Mg_2Si composites with Fe as the control group. *$P < 0.05$. The direct peeling off of Fe matrix was marked by arrows.

elements further confirmed the corrosion of Fe and the hydrolysis of Mg_2Si. Besides, a small amount of Ca and P was also detected, which was beneficial to the recovery of bone tissue since these elements were important components of new bone. Interestingly, some of the un-corroded Fe was surrounded by the corrosion products and fell off the matrix, as marked by the arrow in **Figure 7D,E**. This indicated that the solution had penetrated into the interior of Fe matrix, which greatly accelerated the degradation rate of Fe matrix during the corrosion process. It could be reasonably expected that these corrosion would start with hydrolyzed Mg_2Si and then propagated along the grain boundary direction so that the matrix would continuously corrode and peel off. As a result, Fe/Mg_2Si composites possessed a larger corroded depth than Fe, as shown in **Figure 7F**. This was especially important for Fe, since its slow corrosion rate did not match the growth rate of new bone, which would seriously hamper bone repair. In this study, it was noteworthy that Mg_2Si not only accelerated the initial corrosion of Fe but also broke down the protective degradation product layers, thereby maintaining a rapid corrosion rate.

The calculated degradation rates of Fe/Mg_2Si composites with that of Fe as a control group after immersion for 21 days in SBF are exhibited in **Figure 8A**. It could be found that the degradation rates of the Fe/Mg_2Si composites (0.15 ± 0.013, 0.21 ± 0.015, 0.31 ± 0.021, and 0.33 ± 0.030 mm/y for Fe/0.3Mg_2Si, Fe/0.6Mg_2Si, Fe/0.9Mg_2Si, and Fe/1.2Mg_2Si, respectively) were obviously

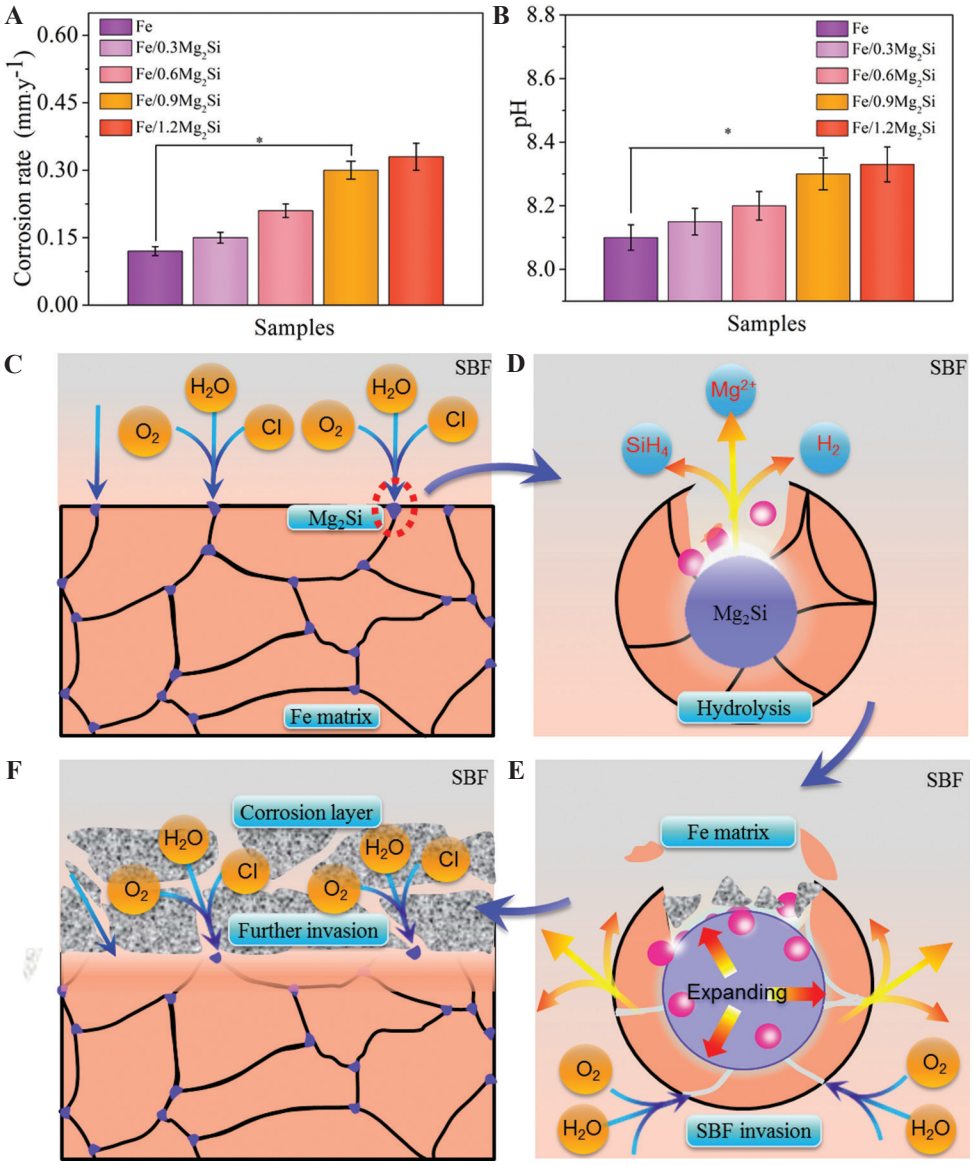

Figure 8. (A) Degradation rates determined by immersion tests and (B) the corresponding pH of Fe/Mg_2Si composites with Fe as a control group in SBF for 21 days. Schematic diagrams of degradation mechanism for Fe/Mg_2Si composites: (C) initial corrosion reaction, (D) Mg_2Si hydrolysis to expose more surface to SBF, (E) hydrolysate escaping from Fe matrix and offering access to SBF, and (F) corrosion propagation as a result of the broken down degradation product layers.

higher than that of Fe (0.12 ± 0.011 mm/y) and the degradation rate increased with the increasing content of Mg_2Si in the composites. This trend was explained by the decomposition of Mg_2Si in the SBF through a chemical reaction with H_2O[45,46]. It should be stated that the degradation rates of Fe/0.9Mg_2Si and Fe/1.2Mg_2Si composites were among 0.2 – 0.5 mm/y, which was a suitable degradation rate to match the restoration process of new bone[2,47]. These results accorded well with that of electrochemical tests. However, it should be remembered that the addition of 1.2 wt% Mg_2Si into the Fe matrix led to a significant decline in mechanical properties. As a result, further increase in the contents of Mg_2Si may be undesirable, especially considering the load-bearing capacity during bone repair. Besides, the pH of Fe/Mg_2Si composites and Fe after immersion for 21 days showed the same trend with the degradation rates, as depicted in **Figure 8B**. The high pH values of

Fe/Mg_2Si composites were caused by the rapid degradation of the Fe matrix.

As biodegradable composites, the degradation rate needs to be consistent with the healing rate of the defect bones to allow a gradual transfer of load to the new bone and to avoid the long-term negative effects of permanent implants. After exposure to physiological environment, Fe degraded in a manner of oxygen absorption corrosion mode, producing degradation products as follows:

$$2Fe \rightarrow 2Fe^{2+} + 4e^- \quad (1)$$

$$O_2 + 2H_2O + 4e^- \rightarrow 4OH^- \quad (2)$$

$$2Fe + 2H_2O + O_2 \rightarrow 2Fe(OH)_2\downarrow \quad (3)$$

$$Fe^{2+} \rightarrow Fe^{3+} + e^- \quad (4)$$

$$Fe^{3+} + 3OH^- \rightarrow Fe(OH)_3\downarrow \quad (5)$$

$$Fe(OH)_2 + 2Fe(OH)_3 \rightarrow Fe_3O_4\downarrow + 4H_2O \quad (6)$$

Reactions between Fe^{2+} from anodic oxidation and other anions in physiological environment could simultaneously occur[39,48]:

$$3Fe^{2+} + 2PO_4^{3-} + 8H_2O \rightarrow Fe_3(PO_4)_2\cdot 8H_2O\downarrow \quad (7)$$

Degradation products, such as $Fe(OH)_2$, $Fe(OH)_3$, Fe_3O_4, and $Fe_3(PO_4)_2\cdot 8H_2O$, were almost insoluble in the physiological environment[49,50]. As a result, the degradation products would deposit on Fe matrix and form dense product layers, as shown in **Figure 7A**, significantly reducing the degradation rates. In this study, Mg_2Si with high chemical activity was introduced into the Fe matrix and it would be readily hydrolyzed according to Equation (8):

$$Mg_2Si + 4H_2O \rightarrow 2Mg(OH)_2 + SiH_4\uparrow \quad (8)$$

The generated gas (SiH_4) would escape from the matrix and then diffuse into the solution, which destroyed the accumulated degradation product layers. Once the protective layers were broken down, the corrosive solution would quickly infiltrate and induce Fe corrosion. More importantly, the generated SiH_4 underwent further hydrolysis:

$$SiH_4 + 2H_2O \rightarrow SiO_2 + 4H_2\uparrow \quad (9)$$

This also aggravated the damage to degradation product layers and hindered the accumulation of the degradation product layers, further enlarging the access of corrosive solution to the matrix. Meanwhile, the produced silicon dioxide (SiO_2) acted as a cathode site, and then galvanic corrosion occurred between SiO_2 and Fe matrix due to the different corrosion potentials.

Based on this corrosion mode, the hydrolysis of Mg_2Si would, on the one hand, create vacancies in the matrix, exposing more surface of Fe to the solution during the initial immersion. On the other hand, the produced gases by the hydrolysis had an expansive effect, which cracked the degradation product layers as well as Fe matrix, and brought about the breakdown of degradation product layers, thereby contributing to the corrosion propagation toward the interior of the matrix. As a result, the degradation product layers became porous, loose and easily detached from the matrix, resulting in peeling off of corrosion products or even Fe matrix, as evidenced in **Figure 7D,E**. Moreover, since Mg_2Si was homogeneously distributed in the Fe matrix, fast and macroscopical corrosion would occur throughout the matrix. This corrosion mechanism was first proposed and verified in this study, which fundamentally solved the problem that corrosion product accumulation hindered the degradation. It should be noted that the generated gases by the hydrolysis of Mg_2Si would be carried away by the circulating blood in the human body, which would not produce obvious side effects.

3.6 Cytocompatibility

Cytocompatibility tests using MG-63 cells were taken to evaluate the biological safety of Fe/0.9Mg_2Si composite. Fluorescent images in extracts were taken to investigate the growth of MG-63 cells, as exhibited in **Figure 9A-D**. It could be found that there was no obvious difference in cell morphologies after 72 h of exposure to different extracts. The average cell number was estimated by ImageJ software according to the fluorescent images in **Figure 9E**, which showed no significant difference. Besides, cell viability was

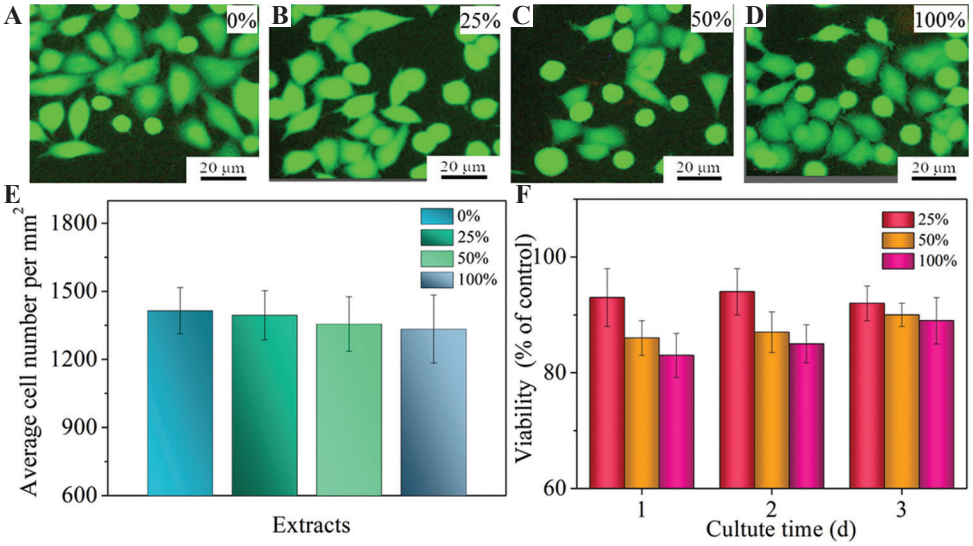

Figure 9. Cytocompatibility of Fe/0.9Mg_2Si composite: fluorescent images of different concentrations of extract: (A) 0%, (B) 25%, (C) 50%, and (D) 100%, respectively, (E) average MG-63 cell number per mm^2 in different concentrations of extracts (25, 50, and 100%, respectively) measured by ImageJ software; (F) MG-63 cell viability after incubation in different concentrations of extracts (25, 50, and 100%, respectively) for 1, 2, and 3 days.

further investigated, and the results are depicted in **Figure 9F**. It was found that cell viability decreased with the increase in concentrations of extract at 1 and 2 days. Meanwhile, there was no statistical significance in the cell viability of Fe/0.9Mg_2Si composite in comparison with the control group. However, on day 3, cell viability of 50 and 100% extracts became approximately identical as that of the control group (0% extract). Moreover, during 3 days of incubation, cell viability was all above 70%, indicating no cytotoxicity of Fe/Mg_2Si composites according to the ISO10993-5[51].

4 Conclusions

In this study, Fe/Mg_2Si composites were successfully fabricated by selective laser melting to accelerate degradation for biomedical applications. The effects of Mg_2Si on microstructure, mechanical properties, and corrosion behaviors of Fe were systematically studied.

(1) Fe/Mg_2Si composites had similar microstructure, in which Mg_2Si was easily discernible with the increase in Mg_2Si content. However, when the additional content of Mg_2Si was 1.2 wt.%, micropores were found.

(2) The addition of Mg_2Si led to a decrease in compression strength, but their compression strength was in the range of compact bone (90 – 170 MPa). The hardness of Fe/0.9Mg_2Si composite (145 HV) was higher than other samples (112, 134, 142, and 127 HV for Fe, Fe/0.3Mg_2Si, Fe/0.6Mg_2Si, and Fe/1.2Mg_2Si, respectively). A slight decrease was found after adding Mg_2Si to 1.2 wt% may be caused by micropores in the microstructure.

(3) Electrochemical tests revealed accelerated corrosion behaviors for Fe/Mg_2Si composites. This was due to the hydrolysis of Mg_2Si, resulting in more matrix exposure to SBF. Immersion tests showed that corrosion occurred in the interior of Fe/Mg_2Si composites with porous and loose corrosion product layers. This induced corrosion propagation toward the interior of the Fe matrix and bulk Fe matrix may peel off. As a result, Fe/Mg_2Si composites exhibited high degradation rates (higher than 0.30 mm/year). *In vitro*, MG-63 cell tests confirmed the good cytocompatibility Fe/Mg_2Si composites. These results collectively showed that hydrolytic expansion was an effective strategy to accelerate the degradation of Fe-based implants for bone applications.

Acknowledgments

This study was supported by the following funds: (1) The Natural Science Foundation of China (51705540, 51935014, 51905553, 81871494, 81871498); (2) Hunan Provincial Natural Science Foundation of China (2018JJ3671, 2019JJ50774, 2019JJ50588); (3) JiangXi Provincial Natural Science Foundation of China (20192ACB20005); (4) Guangdong Province Higher Vocational Colleges and Schools Pearl River Scholar Funded Scheme (2018); (5) The Open Sharing Fund for the Large-scale Instruments and Equipments of Central South University; and (6) The Project of Hunan Provincial Science and Technology Plan (2017RS3008).

References

1. Gao C, Yao M, Li S, *et al*., 2019, Highly Biodegradable and Bioactive Fe-Pd-Bredigite Biocomposites Prepared by Selective Laser Melting. *J Adv Res*, 20:91–104. DOI: 10.1016/j.jare.2019.06.001.
2. Shuai C, Li S, Peng S, *et al*., 2019, Biodegradable Metallic Bone Implants. *Mater Chem Front*, 3(1):544–62. DOI: 10.1039/C8QM00507A.
3. Yang YY, He C, Dianyu E, *et al*., 2019, Mg Bone Implant: Features, Developments and Perspectives. *Mater Design*, 185:108259. DOI: 10.1016/j.matdes.2019.108259.
4. Gao C, Yao M, Shuai C, *et al*., 2019, Nano-SiC Reinforced Zn Biocomposites Prepared Via Laser Melting: Microstructure, Mechanical Properties and Biodegradability. *J Mater Sci Tech*, 35:2608–17. DOI: 10.1016/j.jmst.2019.06.010.
5. Shuai C, Yang W, He C, *et al*., 2019, A Magnetic Micro-Environment in Scaffolds for Stimulating Bone Regeneration. *Mater Des*, 185:108275. DOI: 10.1016/j.matdes.2019.108275.
6. Wang G, Qi F, Yang W, *et al*., 2019, Crystallinity and Reinforcement in Poly-L-Lactic Acid Scaffold Induced by Carbon Nanotubes. *Advances in Polymer Technology*, 2019:10. DOI: 10.1155/2019/8625325.
7. He S, Yang S, Zhang Y, *et al*., 2019, LncRNA ODIR1 Inhibits Osteogenic Differentiation of hUC-MSCs Through the FBXO25/H2BK120ub/H3K4me3/OSX axis. *Cell Death Dis*, 10:1–16. DOI: 10.1038/s41419-019-2148-2.
8. Zivic F, Grujovic N, Pellicer E, *et al*., 2018, Biodegradable Metals as Biomaterials for Clinical Practice: Iron-Based Materials, Biomaterials in Clinical Practice. Springer, Berlin. pp. 225–80. DOI: 10.1007/978-3-319-68025-5_9.
9. Deng Y, Yang Y, Gao C, *et al*., 2018, Mechanism for Corrosion Protection of β-TCP Reinforced ZK60 Via Laser Rapid Solidification. *Int J Bioprint*, 4(1):27–41. DOI: 10.18063/IJB.v4i1.124.
10. Hermawan H, Dubé D, Mantovani D, 2007, Development of Degradable Fe-35Mn Alloy for Biomedical Application. *Adv Mater Res*, 15:107–12. DOI: 10.4028/www.scientific.net/AMR.15-17.107.
11. Schinhammer M, Steiger P, Moszner F, *et al*. 2013, Degradation Performance of Biodegradable FeMnC (Pd) Alloys. *Mater Sci Eng C*, 33:1882–93. DOI: 10.1016/j.msec.2012.10.013.
12. Zhou J, Yang Y, Alonso Frank M, *et al*., 2016, Accelerated Degradation Behavior and Cytocompatibility of Pure Iron Treated with Sandblasting. *ACS Appl Mater Interfaces*, 8:26482–92. DOI: 10.1021/acsami.6b07068.
13. Moravej M, Purnama A, Fiset M, *et al*., 2010, Electroformed Pure Iron as a New Biomaterial for Degradable Stents: *In Vitro* Degradation and Preliminary Cell Viability Studies. *Acta Biomater*, 6:1843–51. DOI: 10.1016/j.actbio.2010.01.008.
14. Jiang W, Wang J, Yu W, *et al*., 2019, *In Situ* Formation of a Gradient Mg2Si/Mg Composite with Good Biocompatibility. *Surf Coat Technol*, 361:255–62. DOI: 10.1016/j.surfcoat.2018.12.107.
15. Sikora-Jasinska M, Paternoster C, Mostaed E, *et al*., 2017, Synthesis, Mechanical Properties and Corrosion Behavior of Powder Metallurgy Processed Fe/Mg2Si Composites for Biodegradable Implant Applications. *Mater Sci Eng C*, 81(2):511–21. DOI: 10.1016/j.msec.2017.07.049.
16. Lee JY, An J, Chua CK, 2017, Fundamentals and Applications of 3D Printing for Novel Materials. *Appl Mater Today*, 7:120–33. DOI: 10.1016/j.apmt.2017.02.004.
17. An J, Teoh JEM, Suntornnond R, *et al*., 2015, Design and 3D Printing of Scaffolds and Tissues. *Engineering*, 1:261–68. DOI: 10.15302/J-ENG-2015061.
18. Sing SL, Huang S, Yeong WY, 2020, Effect of Solution Heat Treatment on Microstructure and Mechanical Properties of Laser Powder Bed Fusion Produced Cobalt-28chromium-6molybdenum. *Mater Sci Eng A*, 769:138511. DOI: 10.1016/j.msea.2019.138511.
19. Nasab MH, Giussani A, Gastaldi D, *et al*., 2019, Effect of Surface and Subsurface Defects on Fatigue Behavior of AlSi10Mg Alloy Processed by Laser Powder Bed Fusion (L-PBF). *Metals*, 9:1063. DOI: 10.3390/met9101063.
20. Yu W, Sing S, Chua C, *et al*., 2019, Particle-Reinforced Metal Matrix Nanocomposites Fabricated by Selective Laser Melting: A State of the Art Review. *Prog Mater Sci*,

104:330-379. DOI: 10.1016/j.pmatsci.2019.04.006.

21. Dadbakhsh S, Mertens R, Hao L, *et al*., 2019, Selective Laser Melting to Manufacture "*In Situ*" Metal Matrix Composites: A Review. *Adv Eng Mater*, 21:1801244. DOI: 10.1002/adem.201801244.
22. Hariharan K, Arumaikkannu G, 2016, Structural, Mechanical and *In Vitro* Studies on Pulsed Laser Deposition of Hydroxyapatite on Additive Manufactured Polyamide Substrate. *Int J Bioprint*, 2:85–94. DOI: 10.1016/S0021-9290(06)83793-0.
23. Lepowsky E, Tasoglu S, 2018, 3D Printing for Drug Manufacturing: A Perspective on the Future of Pharmaceuticals. *Int J Bioprint*, 4:119. DOI: 10.18063/IJB.v4i1.119.
24. Yap CY, Chua CK, Dong ZL, *et al*., 2015, Review of Selective Laser Melting: Materials and Applications. *Appl Phys Rev*, 2:041101. DOI: 10.1063/1.4935926.
25. Loh LE, Chua CK, Yeong WY, *et al*., 2015, Numerical Investigation and an Effective Modelling on the Selective Laser Melting (SLM) Process with Aluminium Alloy 6061. *Int J Heat Mass Transfer*, 80:288–300. DOI: 10.1016/j.ijheatmasstransfer.2014.09.014.
26. Sun Z, Tan X, Tor SB, *et al*. 2018, Simultaneously Enhanced Strength and Ductility for 3D-Printed Stainless Steel 316L by Selective Laser Melting. *NPG Asia Materials*, 10:127. DOI: 10.1038/s41427-018-0018-5.
27. Li Y, Zhou K, Tan P, *et al*., 2018, Modeling Temperature and Residual Stress Fields in Selective Laser Melting. *Int J Mech Sci*, 136:24–35. DOI: 10.1016/j.ijmecsci.2017.12.001.
28. Yu W, Sing SL, Chua CK, *et al*., 2019, Influence of Re-Melting on Surface Roughness and Porosity of AlSi10Mg Parts Fabricated by Selective Laser Melting. *J Alloys Compd*, 792:574–81. DOI: 10.1016/j.jallcom.2019.04.017.
29. Kuo C, Chua C, Peng P, *et al*., 2019, Microstructure Evolution and Mechanical Property Response Via 3D Printing Parameter Development of Al-Sc alloy. *Virtual Phys Prototyp*, 15:1–10. DOI: 10.1080/17452759.2019.1698967.
30. Vanarase AU, Muzzio FJ, 2011, Effect of Operating Conditions and Design Parameters in a Continuous Powder Mixer. *Powder Technol*, 208:26–36. DOI: 10.1016/j.powtec.2010.11.038.
31. Portillo PM, 2008, Quality by Design for Continuous Powder Mixing. Rutgers University-Graduate School, New Brunswick.
32. Shuai C, Zan J, Yang Y, *et al*., 2019, Surface Modification Enhances Interfacial Bonding in PLLA/MgO Bone Scaffold. *Mater Sci Eng C*, 108:110486. DOI: 10.1016/j.msec.2019.110486.
33. Shuai C, Xu Y, Feng P, *et al*., 2019, Antibacterial Polymer Scaffold Based on Mesoporous Bioactive Glass Loaded with *In Situ* Grown Silver. *Chem Eng J*, 374:304–15. DOI: 10.1016/j.cej.2019.03.273.
34. Wang S, Xu Y, Zhou J, *et al*., 2017, *In Vitro* Degradation and Surface Bioactivity of Iron-Matrix Composites Containing Silicate-Based Bioceramic. *Bioact Mater*, 2:10–18. DOI: 10.1016/j.bioactmat.2016.12.001.
35. Shuai C, Li S, Wang G, *et al*., 2019, Strong Corrosion Induced by Carbon Nanotubes to Accelerate Fe Biodegradation. *Mater Sci Eng C*, 104(5):109935. DOI: 10.1016/j.msec.2019.109935.
36. Wang H, Zheng Y, Li Y, *et al*., 2017, Improvement of *In Vitro* Corrosion and Cytocompatibility of Biodegradable Fe Surface Modified by Zn Ion Implantation. *Appl Surf Sci*, 403(12):168–76. DOI: 10.1016/j.apsusc.2017.01.158.
37. Shuai C, Cheng Y, Yang Y, *et al*., 2019, Laser Additive Manufacturing of Zn-2Al Part for Bone Repair: Formability, Microstructure and Properties. *J Alloys Comp*, 798:606–15. DOI: 10.1016/j.jallcom.2019.05.278.
38. Cheng J, Liu B, Wu Y, *et al*., 2013, Comparative *In Vitro* Study on Pure Metals (Fe, Mn, Mg, Zn and W) as Biodegradable Metals. *J Mater Sci Tech*, 29:619–27. DOI: 10.1016/j.jmst.2013.03.019.
39. Shuai C, Liu G, Yang Y, *et al*., 2019, Functionalized BaTiO3 Enhances Piezoelectric Effect Towards Cell Response of Bone Scaffold. *Colloids Surf*, 3:110587–94. DOI: 10.1016/j.colsurfb.2019.110587.
40. Feng P, Kong Y, Yu L, *et al*., 2019, Molybdenum Disulfide Nanosheets Embedded with Nanodiamond Particles: Co-Dispersion Nanostructures as Reinforcements for Polymer Scaffolds. *Appl Mater Today*, 17:216–26. DOI: 10.1016/j.apmt.2019.08.005.
41. Prakasam M, Locs J, Salma-Ancane K, *et al*., 2017, Biodegradable Materials and Metallic Implants a Review. *J Funct Biomater*, 8:44. DOI: 10.3390/jfb8040044.
42. Gao C, Peng S, Feng P, *et al*., 2017, Bone Biomaterials and Interactions with Stem Cells. *Bone Res*, 5:17059. DOI: 10.1038/boneres.2017.59.
43. Dehestani M, Adolfsson E, Stanciu LA, 2016, Mechanical Properties and Corrosion Behavior of Powder Metallurgy Iron-Hydroxyapatite Composites for Biodegradable Implant Applications. *Mater Des*, 109:556–69. DOI: 10.1016/j.matdes.2016.07.092.
44. Kato K, Ochiai S, Yamamoto A, *et al*., 2013, Novel Multilayer Ti Foam With Cortical Bone Strength and Cytocompatibility. *Acta Biomater*, 9:5802–09. DOI:

10.1016/j.actbio.2012.11.018.

45. Panemangalore DB, Shabadi R, Tingaud D, *et al*., 2019, Biocompatible Silica-Based Magnesium Composites. *J Alloys Comp,* 772(15):49–57. DOI: 10.1016/j.jallcom.2018.09.060.
46. Zhang Y, Wang L, Sun W, *et al*., 2019, Membrane Technologies for Li+/Mg2+ Separation From Salt-Lake Brines and Seawater: A Comprehensive Review. *J Ind Eng Chem,* 81:7–23. DOI: 10.1016/j.jiec.2019.09.002.
47. Bowen PK, Shearier ER, Zhao S, *et al*., 2016, Biodegradable Metals for Cardiovascular Stents: From Clinical Concerns to Recent Zn-Alloys. *Adv Healthc Mater*, 5:1121–40. DOI: 10.1002/adhm.201501019.
48. Shuai C, Yang Y, Feng P, *et al*., 2018, A Multi-Scale Porous Scaffold Fabricated by a Combined Additive Manufacturing and Chemical Etching Process for Bone Tissue Engineering. *Int J Bioprint*, 4:133. DOI: 10.18063/IJB.v4i2.133.
49. Gorejová R, Haverová L, Oriňaková R, *et al*., 2019, Recent Advancements in Fe-Based Biodegradable Materials for Bone Repair. *J M Sci*, 54(12):1913–47. DOI: 10.1007/s10853-018-3011-z.
50. Jin J, Tan Y, Liu R, *et al*., 2018, Synergy Effect of Attapulgite, Rubber, and Diatomite on Organic Montmorillonite-Modified Asphalt. *J Mater Civil Eng*, 31:04018388. DOI: 10.1061/(ASCE)MT.1943-5533.0002601.
51. Zhao Y, Jamesh MI, Li WK, *et al*., 2014, Enhanced Antimicrobial Properties, Cytocompatibility, and Corrosion Resistance of Plasma-Modified Biodegradable Magnesium Alloys. *Acta Biomater*, 10:544–56. DOI: 10.1016/j.actbio.2013.10.012.